JOURNAL OF AIRCRAFT
Vol. 44, No. 1, January–February 2007

Design and Numerical Optimization of Thick Airfoils Including Blunt Trailing Edges

T. Winnemöller*
RWTH Aachen University, 52062 Aachen, Germany
and
C. P. van Dam†
University of California, Davis, Davis, California 95616

DOI: 10.2514/1.23057

The numerical optimization of thick airfoils by means of genetic- and gradient-based numerical optimization in combination with a Navier–Stokes code is described and the results are discussed. The objectives of the study are to maximize both the section moment of inertia, and the airfoil lift-to-drag ratio at fully turbulent conditions and a chord Reynolds number of 1×10^6. A robust and flexible airfoil surface definition that is based on polynomial functions and allows for blunt trailing edges is used to generate section shapes with a maximum-thickness-to-chord ratio between 35 and 42%. To mitigate the unsteady vortex shedding, a splitter plate is added to the blunt trailing edge of the resulting airfoils. This allows steady-state simulations with the Navier–Stokes code and reduces the calculation time. The study resulted in a Pareto front, which represents a range of aerodynamically and structurally improved airfoils. Although the optimizer was given the opportunity to create airfoils with a nominally sharp trailing edge, the improved airfoils all contain significant trailing-edge thickness.

Nomenclature

C_d	=	drag coefficient
C_l	=	lift coefficient
C_p	=	pressure coefficient
c	=	chord length
I_x	=	sectional moment of inertia
Re	=	Reynolds number
$r_{\text{le},l}$	=	leading edge radius lower surface
$r_{\text{le},u}$	=	leading edge radius upper surface
spt	=	splitter plate thickness
t	=	airfoil thickness
t_{te}	=	trailing edge thickness
teg	=	trailing edge gradient/direction
tew	=	trailing edge wedge angle
X	=	Cartesian coordinate x normalized by the chord length, x/c
$x_{l,\max}$	=	chord location of lower crest
$x_{u,\max}$	=	chord location of upper crest
Z	=	Cartesian coordinate z normalized by the chord length, z/c
$z_{l,\max}$	=	ordinate of lower crest
$z_{u,\max}$	=	ordinate of upper crest
α	=	angle of attack

I. Introduction

STRUCTURAL strength, stiffness, and/or volume demands may require the application of thick airfoils for wings and rotors. Unfortunately thick airfoils (i.e., airfoils with a maximum-thickness-to-chord ratio, $t/c > 0.25$) with sharp trailing edges have relatively poor aerodynamic performance, especially when, as a result of surface contamination, the boundary-layer transitions from the laminar to the turbulent state near the leading edge. Premature loss of laminar flow leads to an increase in drag, but also a loss in lift, particularly a decrease in maximum lift. To improve the aerodynamic performance of thick airfoils and minimize their sensitivity to premature transition, blunt trailing edges have been proposed [1–3].

Standish et al. [3,4] conducted studies on blunt trailing edge airfoils, and their results show that the incorporation of a blunt trailing edge can benefit both the aerodynamic and the structural performance of thick airfoils. The latter benefits from the increased moment of inertia, whereas the former benefits from the reduced sensitivity of the lift to premature boundary-layer transition. Unfortunately blunt trailing edges also increase the drag coefficient, but there are several design options to decrease the base drag penalty. For example, Tanner [5,6] proposed the use of a splitter plate to alleviate vortex shedding at the blunt base, and create a more steady flow, with a lower base drag penalty and reduced force fluctuations. Based on the findings of these studies, the blunt trailing edge appears to be a promising concept to increase the performance of thick airfoils.

The study by Standish et al. [3,4] involved incorporating a blunt trailing edge by modifying existing airfoils and analyzing the aerodynamic characteristics of the resulting configurations with little attention to maximizing airfoil performance for given conditions. As a result of recent improvements in computer hardware and software, as well as in computational fluid dynamic (CFD) methods for the solution of the steady and time-accurate Navier–Stokes equations, it is possible to accurately predict the flow about complex-shaped airfoils such as blunt trailing edge airfoils, and their performance characteristics in a sufficiently short time to allow numerical optimization on modestly sized PC clusters. The goal of this project is to design and optimize thick airfoils using CFD and a combination of zero-order (genetic) and first-order (gradient-based) numerical optimization methods. The airfoil design variables are based on some type of surface definition of the airfoil, requiring the study of various surface definition options including trailing edge thickness. The use of the additional design freedom gained from allowing the trailing edge to be blunt has previously been limited to the optimization of airfoils operating at transonic and supersonic flow conditions. The results from the present study demonstrate that blunt trailing edges may also be beneficial in the design of thick subsonic airfoils.

Presented as Paper 238 at the 44th AIAA Aerospace Sciences Meeting and Exhibit, Reno, Nevada, 9–12 January 2006; received 8 February 2006; revision received 30 August 2006; accepted for publication 25 July 2006.

*Currently Graduate Student Researcher, Institute of Aerodynamics. AIAA Student Member.

†Professor, Department of Mechanical and Aeronautical Engineering. AIAA Senior Member.

In the following section the numerical methods used in this study are outlined including the airfoil surface generation, the grid generation for the integration domain, the flow solver, and the genetic and gradient-based numerical optimization techniques. Next, several relevant results validating the flow solver and solution methodology are presented. The third section outlines the optimization process including the multidisciplinary objective function and the design constraints used in this study. This is followed by the results in the form of a Pareto front and detailed analysis and comparison of the aerodynamic and structural characteristics of several airfoil designs.

II. Numerical Methods

A. Surface Generation

A surface definition based on polynomial functions, similar to Sobieczky's PARSEC [7] was used to create the airfoil shapes. The geometry parameters to define the airfoil shape are

1) upper/lower leading edge radius ($r_{\text{le},u}$, $r_{\text{le},l}$)
2) chordwise location of upper/lower crest ($x_{u,\max}$, $x_{l,\max}$)
3) ordinate of upper/lower crest ($z_{u,\max}$, $z_{l,\max}$)
4) thickness of trailing edge (t_{te})
5) trailing edge direction (teg)
6) trailing edge wedge angle (tew).

The main difference between the PARSEC airfoil geometry definition and the definition used in the present study is the exclusion of the upper and lower crest surface curvature parameters. Surface curvature is particularly important in the optimization of transonic airfoils but found to be of lesser importance for the subsonic airfoils in the present study. Also, the curvature parameter was found to severely reduce numerical optimization convergence.

The listed geometric parameters are used to determine the coefficients a_1 through a_5 of the polynomial function

$$Z = \sum_{n=1}^{5} a_n \cdot X^{n-\frac{1}{2}} \tag{1}$$

Separate polynomials are used to define the upper and lower surfaces of the airfoil. The leading edge radii are used to calculate a_1:

$$a_1 = \sqrt{\frac{1}{2} r_{\text{le}}} \tag{2}$$

This is derived from the surface definition used for the NACA four-digit airfoil series [8].

B. Grid Generation

After generating the airfoil shape with the algorithm described above, a grid was generated. The first step was the choice of the general grid shape with C and O grids the obvious choices. For sharp trailing edge airfoils, a C grid tends to keep cell skewness minimal and the angles in the cells close to 90 deg. When the trailing edge becomes blunt, cell skewness increases and areas of grid clustering appear in the near wake region. The O grid in contrast works well for blunt trailing edge configurations. When a splitter plate is added to the blunt base, additional regions with dense grid clustering appear in the C grid. Unfortunately the splitter plate causes clustering problems even in the O grid (Fig. 1), but still this grid configuration was considered the better choice for meshing thick airfoils (with and without blunt trailing edge) and was used throughout the study.

A hyperbolic grid generator was used to generate the O grid. The normal spacing depends on the Reynolds number, because the utilized Spalart–Allmaras turbulence model [9] works best with an initial spacing of $y+ \approx 1$. For $Re = 1 \times 10^6$ this condition results in an initial spacing of $z_1 = 1.8 \times 10^{-5}$. The spacing is constant for the first five cells, and then the grid stretches out to $0.03c$ off the surface with the next 30 points. Another 50 points are used to stretch the grid to a full chord length off the surface, and finally 30 points are used from one chord length to $50c$. This results in a total of 125 grid points normal to the surface, with a far-field distance of 50 chord lengths.

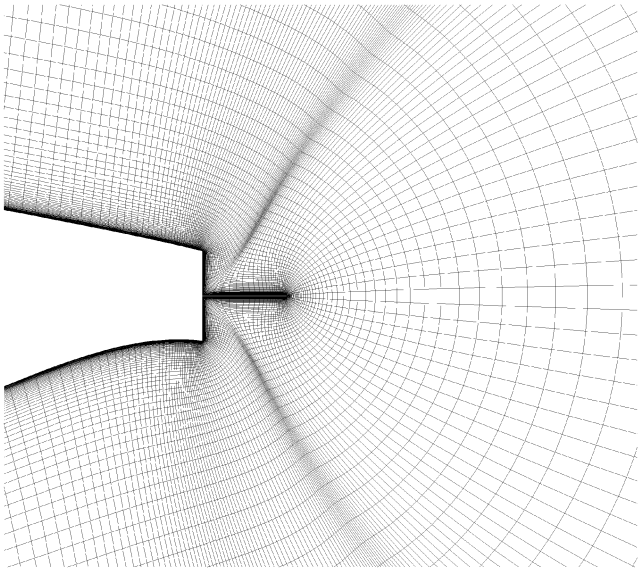

Fig. 1 O grid at a blunt trailing edge with splitter plate.

C. Flow Solver

The flow solver ARC2D was developed by Pulliam and Steger at the NASA Ames Research Center [10].[‡] The code solves the compressible, two-dimensional, Reynolds-averaged Navier–Stokes (RANS) equations in strong conservation-law form. The governing equations in generalized curvilinear coordinates are central differenced in standard second-order form and solved using the implicit Beam–Warming approximate factorization scheme [11]. Artificial dissipation terms are added for numerical stability with the second order dissipation coefficient = 0.00 and the fourth order scalar dissipation coefficient = 0.64. The code employs local time stepping and mesh sequencing to accelerate convergence of steady solutions. Time-accurate solutions are obtained using a second-order time advancing scheme with user-specified physical time step, pseudotime step, and number of subiterations. Throughout this project different settings for a number of subiterations in combination with different time steps were tested to achieve temporal convergence. The flow simulations can be conducted at fixed angle of attack or fixed lift coefficient. ARC2D includes different turbulence models with the one-equation Spalart–Allmaras model [9] used throughout this project. The reason for this selection is that this model gave the most accurate results in prior blunt trailing edge airfoil studies [3]. The full ARC2D documentation [10] should be considered for more information on this flow solver.

D. Genetic Algorithm

The genetic algorithm (GA) used in this project is based on the work by Holst and Pulliam [12,13]. It is a two-objective single-point optimization method, which provides the opportunity to collect all of the "best" solutions in the so-called Pareto front. This is necessary because the objectives (maximize lift-to-drag ratio, maximize moment of inertia) of this optimization are contradictory.

All design points on the Pareto front are nondominated, which means, for a design point (f_1^*, f_2^*) on the Pareto front, there can be no points (f_1, f_2) in the design space, such that:

$$\begin{gathered} f1 \geq f1^* \wedge f2 > f2^* \\ \vee \\ f1 > f1^* \wedge f2 \geq f2^* \end{gathered} \tag{3}$$

This means that no airfoil design outside the front is better in both objectives than any airfoil design on the Pareto front. Also, every design on the front is better than all other designs on the Pareto front

[‡]Available at http://people.nas.nasa.gov/~pulliam/mypapers/vki_notes/vki_notes.html [retrieved October 2006].

in one of the two objectives. The advantage of this approach is obvious; the optimization results cover a range of design solutions for objectives A and B. For a given A, the Pareto front provides the design with the best possible B and vice versa.

E. Gradient-Based Optimization Method

The gradient-based optimization method used in this project is based on the information presented by Vanderplaats [14]. Here, the conjugate direction algorithm by Fletcher–Reeves was adopted. The convergence rate of the conjugate direction algorithm is significantly improved over that of the steepest descent algorithm by a simple modification. In this project one-sided differences were used to calculate the gradient. More detailed information on the conjugate direction algorithm as well as the Golden Section algorithm, which was used to perform the one-dimensional search within the conjugate direction method, is provided in [14].

III. Validation

A. Flow Solver ARC2D

The Reynolds-averaged Navier–Stokes code ARC2D has been extensively applied and validated for airfoil analysis [3,15–18].

In this project ARC2D was validated against the wind tunnel results for the thick truncated airfoil FX77-W-343 [19], which is an airfoil with a maximum thickness of 34.3% and a blunt trailing edge with a thickness of 4.2% (Fig. 2). Because of the lack of a transition prediction model in the RANS solver, RANS free transition locations in this study are obtained with transition specified at the locations predicted by using XFOIL [20]. The validation focused on the lift-to-drag ratio, because this is an optimization objective. Figure 3 shows a comparison of the experimental results and the data calculated with ARC2D. The results are generally in good agreement before stall but the poststall behavior is not accurately captured. Additional validations of the ARC2D code as applied to blunt trailing edge airfoils are presented by Standish and van Dam [3].

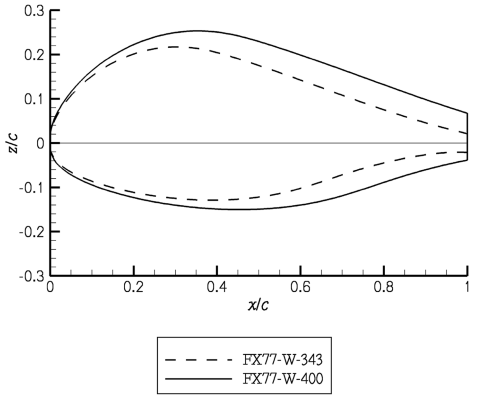

Fig. 2 Geometry of FX77-W-343 and FX77-W-400.

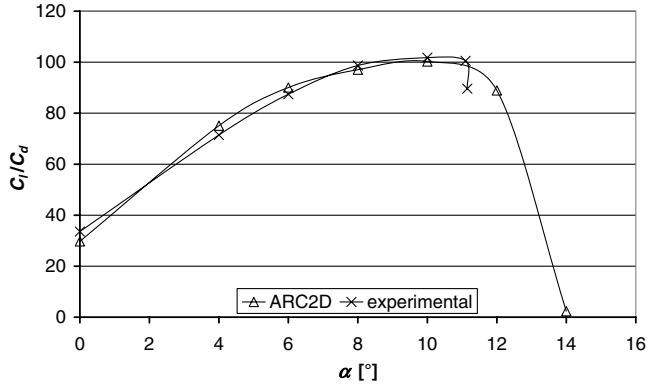

Fig. 3 Lift-to-drag ratios for FX77-W-343, experimental [19], and ARC2D results, $Re = 4 \times 10^6$, $Ma = 0.3$, free transition (transition points calculated with XFOIL [20]).

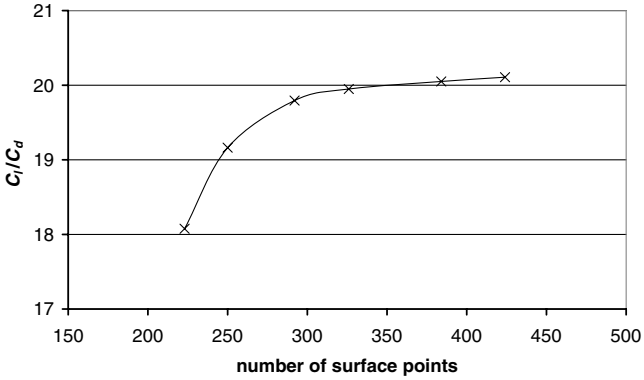

Fig. 4 Comparison of lift-to-drag ratios for different numbers of surface grid points, $Re = 1 \times 10^6$, $Ma = 0.3$, transition at $(x_{\text{upper}}/c) = 0.05$, $(x_{\text{lower}}/c) = 0.05$, steady-state simulation.

To reduce the calculation time, it is necessary to keep the number of grid points at a minimum. This minimum is defined by the number of grid points, which is necessary for ARC2D to generate accurate results. Different grid spacings were tested. Figure 4 shows the resulting lift-to-drag ratios against the number of surface points. Even for 250 surface points the deviation of the lift-to-drag ratio is smaller than 5% compared to those for the finer grid with 424 surface points. For larger spacings the accuracy reduces rather fast, as visible in the difference resulting from a further reduction to 223 surface points. Hence the grid generation settings, which led to 250 surface points in the test case, were chosen for the optimization process. This reduces the calculation time significantly compared to the original setting, whereas the deviation is acceptable. The normal grid spacing is described in Sec. II.

B. Splitter Plate Effectiveness

The unsteady vortex shedding requires a time-accurate solution approach, which is expensive in terms of calculation time. By mitigating the vortex shedding with the help of a splitter plate, the time-accurate simulation can be reduced to a steady-state simulation resulting in significant computational savings.

To realize a steady flow around a blunt trailing edge airfoil in two dimensions Tanner [5,6] suggested the use of a splitter plate which separates the upper surface flow from the lower surface flow in the near wake. To evaluate the effectiveness of the splitter plate, different splitter plate sizes were tested and the results for time-accurate and steady-state simulations were compared. Thin splitter plates appear to work well in terms of mitigating bluff body vortex shedding; therefore a very thin splitter plate with a thickness of 0.1% of the

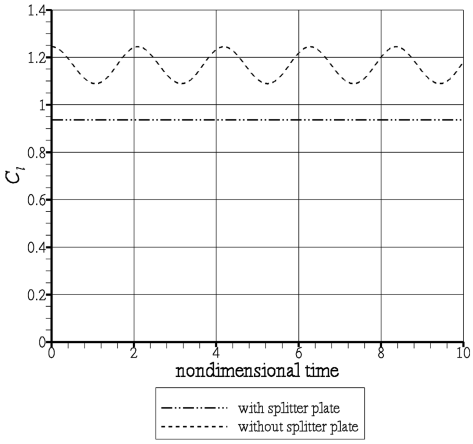

Fig. 5 Lift coefficient of airfoil B against time, $\alpha = 8$ deg, fully turbulent flow, $Re = 1 \times 10^6$, $Ma = 0.3$.

Table 1 Aerodynamic coefficients for airfoil A with a splitter plate, fully turbulent flow, $Re = 1 \times 10^6$, $Ma = 0.3$

α, deg		C_l	C_d	C_l/C_d
5.59	Steady state	1.002	0.0334	30.027
5.59	Time accurate	0.997	0.0341	29.190

Table 2 Aerodynamic coefficients for airfoil B with a splitter plate, fully turbulent flow, $Re = 1 \times 10^6$, $Ma = 0.3$

α, deg		C_l	C_d	C_l/C_d
8.63	Steady state	0.998	0.0398	25.090
8.63	Time accurate	0.994	0.0405	24.545

chord ($spt/c = 0.001$) was chosen for the optimization process. To keep the influence of the splitter plate on the aerodynamic coefficients as small as possible, the splitter plate length was made equal to the trailing edge thickness ($spl = t_{\text{te}}$), which is shown to be an optimum size to mitigate vortex shedding [5,6]. Figure 5 depicts the lift coefficient as a function of time for a blunt trailing edge airfoil (airfoil B, see Sec. V) with and without a splitter plate. The splitter plate is shown to steady the flow and, hence, to mitigate the lift fluctuations. The Strouhal number based on the lift fluctuations observed in Fig. 5 is 0.21, in good agreement with experimentally observed Strouhal numbers for blunt trailing edge airfoils [21]. Tables 1 and 2 present lift and moment results for two thick blunt trailing edge airfoils with splitter plates (these airfoils are discussed in more detail in Sec. V). The results from steady-state and time-accurate simulations are in good agreement, though the lift-to-drag ratio, which is an optimization objective, is slightly higher in the steady-state simulation. Because this occurs consistently, it is not a problem for the optimization, and a splitter plate with a thickness of $0.1\%c$ and a length equal to the trailing edge thickness is selected to mitigate vortex shedding and to allow steady-state simulations.

Throughout the project the aerodynamic coefficients were normalized based on a chord length of unity instead of the actual chord which exceeds one when a splitter plate is added. This constant reference length allows direct comparison of the force and moment coefficients without having to account for changes in actual chord length due to the splitter plate.

IV. Optimization Process

The GA and the gradient method (described in Sec. II) were sequentially applied to exploit the advantages of both approaches. First the conjugate direction method was applied to optimize airfoils with fixed thickness for maximum lift-to-drag ratio. After a given number of iterations (or after the method found a local maximum) the process was stopped and the airfoils were transferred to the GA to provide a basis for the genetic optimization process. The GA carried out a multiobjective optimization for lift-to-drag ratio and moment of inertia resulting in a Pareto front, which will be discussed in Sec. V. Convergence was achieved after 362 generations based on the fact that the Pareto front became stationary.

A. Objective Function

The multiobjective function consists of two parts: the lift-to-drag ratio, which is a measure of the aerodynamic performance of the airfoil, and the moment of inertia, which is a measure of the structural efficiency of the airfoil.

1. *Lift-to-Drag Ratio C_l/C_d*

The lift-to-drag ratio was used as a performance figure for the aerodynamics of the airfoils. It was calculated by evaluating the ARC2D result files, which provide the lift coefficient, C_l, and drag coefficient, C_d, based on airfoil surface integration.

2. *Moment of Inertia*

The sectional moment of inertia of the thin-shelled airfoil structure was used as a measure of structural strength of the airfoil. It is defined as

$$I_x = \int_{x=0}^{x=c} [(z_u - z_{\text{center of mass}})^2 + (z_{\text{center of mass}} - z_l)^2]\,\mathrm{d}x \tag{4}$$

The sectional moment of inertia I_x reflects how well the airfoil can handle wing bending loads. It is calculated with respect to the sectional center of mass and is nondimensionalized by the reference chord length to the power three.

B. Design Conditions

The flow conditions for this study were set to fully turbulent flow over the airfoil at a chord Reynolds number $Re = 1 \times 10^6$ and Mach number $Ma = 0.3$. These conditions nominally match those of the inboard region of a large wind-turbine blade, where thick airfoils are required to mitigate the structural stresses. The Mach number is greater than the Mach numbers generally encountered by the inboard sections of a wind-turbine blade. The reason for this choice is that ARC2D solves the compressible form of the Navier–Stokes equations and, as a result, low Mach number flows ($Ma < 0.2$) cause convergence problems. This increase in the Mach number from nominally about 0.1–0.3 has only a small effect on the computed lift and drag values.

The next step was the definition of the design space. The goal was to optimize thick airfoils, and hence the boundaries were chosen

$$0.35 \le \frac{t}{c} \le 0.42 \tag{5}$$

This thickness is a projected thickness on the y–z plane and not the thickness normal to the camber line. The reason to set boundaries for the thickness is that an unconstrained optimization is just not feasible. A further essential design variable was the trailing edge thickness; its constraints were set to

$$0.005 \le \frac{t_{\text{te}}}{c} \le 0.2 \tag{6}$$

These constraints for the trailing edge thickness allow a wide range of designs, from a nominally sharp trailing edge to a very blunt trailing edge. The other design variables were constrained in a similar way; they allow all reasonable designs and prevent the optimizer wasting time on geometries that do not make sense from an aerodynamic point of view. These are the constraints chosen for the remaining design variables:

$$\begin{aligned} 0.05 \le \frac{z_{u,\max}}{t} < 0.95 \qquad & 0.001 \le r_{\text{le},u} \le 0.25 \\ 0.001 \le r_{\text{le},l} \le 0.25 \qquad & 0.15 \le x_{u,\max} \le 0.6 \\ 0.15 \le x_{l,\max} \le 0.6 \qquad & -30 \le teg \le 30 \ \text{deg} \\ -10 \le tew \le 45 \ \text{deg} \qquad & z_{\text{te}} = 0.00 \end{aligned} \tag{7}$$

The genetic algorithm directly adjusts these variables.

The design parameters for the modified PARSEC (Sec. II) ordinate of upper/lower crest $z_{u,\max}$ and $z_{l,\max}$ result from

$$z_{u,\max} = \frac{z_{u,\max}}{t} \cdot \frac{t}{c} \qquad z_{l,\max} = \left(1 - \frac{z_{u,\max}}{t}\right) \cdot \frac{t}{c} \tag{8}$$

The conjugate direction method uses a slightly different set of design variables. To uncouple upper and lower surfaces, independent trailing edge angles for upper (tea_u) and lower surfaces (tea_l) were implemented. For the surface generation they are transformed into the trailing edge direction and the trailing edge wedge angle

$$tew = tea_l - tea_u \qquad teg = \frac{tew}{2} + tea_u \tag{9}$$

which are used by the modified PARSEC algorithm.

To focus on airfoils that provide acceptable aerodynamic performance, a minimum lift-to-drag ratio of $C_l/C_d = 10$ was set for airfoil selection within the GA. This prevents the optimizer from optimizing for airfoils with very high moment of inertia, but also very high drag. A lift coefficient of $C_l = 1$ was set for the airfoil operating point. Again, this lift condition nominally matches that encountered in the inboard region of a large wind-turbine blade at design load conditions. This means that the angle of attack is continuously adjusted throughout the simulation to maintain the required lift coefficient. Airfoil designs that are unable to generate this lift value due to the existence of separated (stalled) flow are automatically eliminated.

V. Results and Discussion

A. Pareto Front

Figure 6 shows the Pareto front resulting from the genetic optimization. It represents a collection of best airfoils (see Sec. II for more information on the Pareto front) found during the optimization process. Each airfoil on this curve has a unique combination of aerodynamic performance and structural efficiency characteristics and the optimizer found no other airfoil better in both objectives. For a given moment of inertia, I_x, the Pareto front indicates the achievable lift-to-drag ratio for an operating point of $C_l = 1$. The optimization results provide the corresponding airfoil geometry.

Figure 6 includes sketches of representative airfoils on the Pareto front. These airfoil sketches demonstrate that the airfoils with higher lift-to-drag ratios are shaped such that the majority of the thickness is below the chord line. For a lift-to-drag ratio of about 35 the lower boundary for maximum airfoil thickness $t/c = 0.35$ is reached; in the attempt to reach higher lift-to-drag ratios a big decrease in the moment of inertia has to be accepted, as illustrated by the nearly flat top part of the Pareto front. For a lift-to-drag ratio of about 20 the upper boundary for maximum thickness of $t/c = 0.42$ is reached. To reach higher moments of inertia the airfoil shape changes fundamentally and the majority of the thickness moves above the chord line, which is the more classic airfoil design.

B. Airfoil Analysis

In the following section two airfoils from the Pareto front, called airfoil A and airfoil B, will be further analyzed at $Re = 1 \times 10^6$ and fully turbulent conditions. These analyses will be conducted for the airfoils with and without splitter plates.

1. Airfoil A

Airfoil A (Fig. 7) has a projected thickness of 38.2% of the chord length (excluding the splitter plate). The blunt trailing edge has a thickness of $t_{te}/c = 0.095$. The moment of inertia is $I_x = 0.039$. Table 1 compares the ARC2D results for steady-state simulation and for time-accurate simulation. The results are in good agreement.

Figure 8 shows the lift curves for airfoil A with and without a splitter plate. Because of the blunt trailing edge, strong unsteady vortex shedding occurs for airfoil A without a splitter plate. This increases the drag and reduces the maximum lift-to-drag ratio, though the time-averaged lift is higher than for the airfoil with a splitter plate. This higher lift results from the incomplete pressure recovery on the upper surface as explained in more detail in the following section on airfoil B.

Figure 9 depicts the drag polars for the configuration with and without a splitter plate. The version without a splitter plate obviously suffers a drag penalty from unsteady vortex shedding. The drag reduction at around $\alpha = 6$ deg to $\alpha = 8$ deg is due to weaker unsteady vortex shedding at these angles of attack. With unsteady vortex shedding mitigated, the blunt trailing edge drag penalty is smaller at these angles of attack. The lift and drag fluctuations are smaller also.

Figure 10 shows a full oscillation cycle of the unsteady vortex shedding at an angle of attack of $\alpha = 6$ deg. Figure 10a shows a vortex that is just shed from the lower surface side of the blunt base.

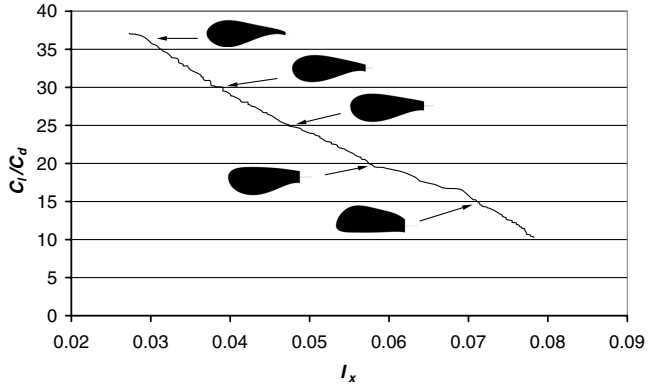

Fig. 6 GA based Pareto front for thick airfoils with splitter plate at fully turbulent conditions, $C_l = 1.0$, $Re = 1 \times 10^6$, $Ma = 0.3$.

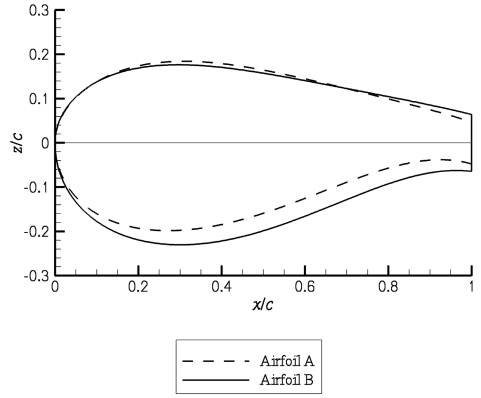

Fig. 7 Geometry of airfoil A and airfoil B.

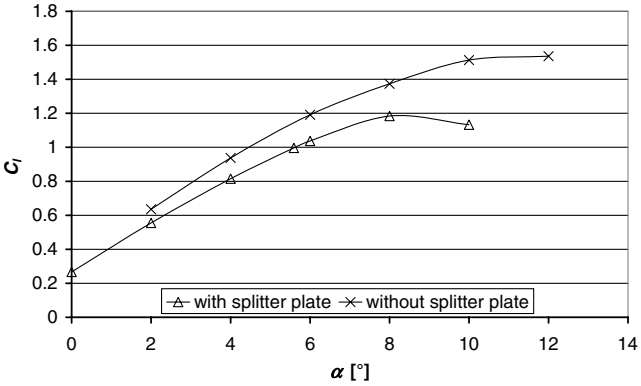

Fig. 8 Lift curves for airfoil A, time-accurate ARC2D simulation, fully turbulent flow, $Re = 1 \times 10^6$, $Ma = 0.3$.

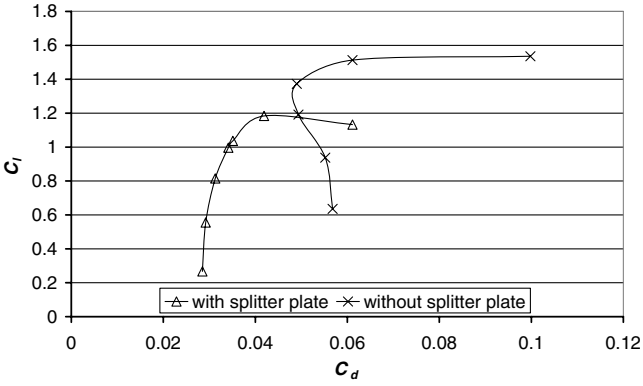

Fig. 9 C_l against C_d polar for airfoil A, time-accurate ARC2D simulation, fully turbulent flow, $Re = 1 \times 10^6$, $Ma = 0.3$.

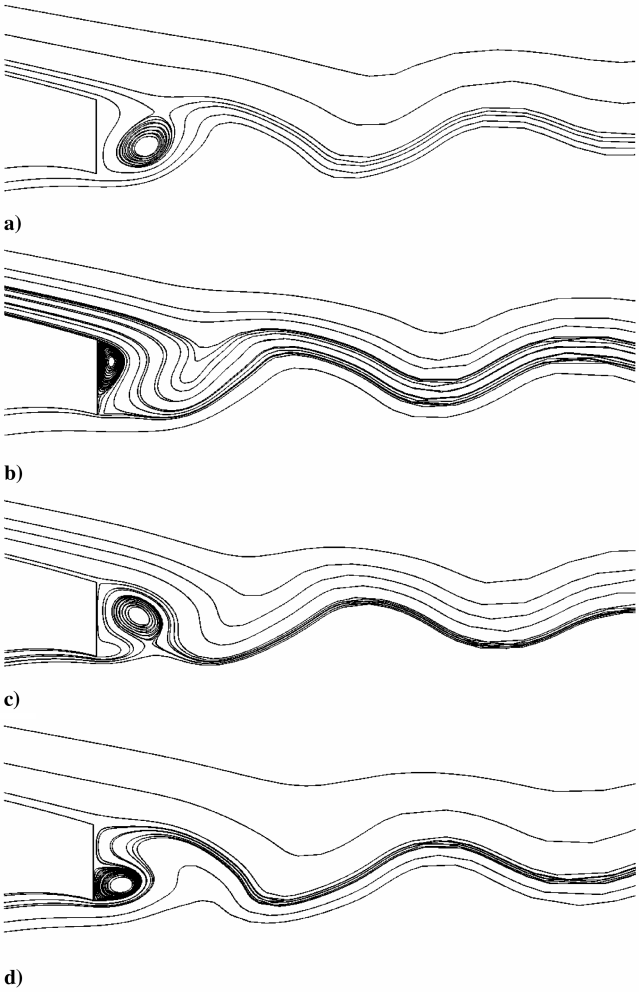

Fig. 10 Flow around the trailing edge of airfoil A, at $\alpha = 6$ deg, fully turbulent flow, $Re = 1 \times 10^6$, $Ma = 0.3$, instantaneous streamlines visualize unsteady vortex shedding at the trailing edge.

Figure 10b shows the flow one-quarter of the oscillation cycle later; a new vortex develops at the upper surface side of the blunt base. Figure 10c shows this vortex shedding from the base. Figure 10d three-quarters of the oscillation cycle later than Fig. 10a shows a vortex developing at the lower surface side of the base. A further quarter of a cycle later, the oscillation is completed, and the flow is again very similar to that depicted in Fig. 10a.

2. *Airfoil B*

The projected thickness of airfoil B is 40.7% of the chord length (Fig. 7). With a trailing edge thickness of $t_{te}/c = 0.129$ the moment inertia of this airfoil is $I_x = 0.0473$. As for airfoil A there is more thickness below the chord line than above. Though airfoil B is thicker than airfoil A, the gradient of the upper surface behind the upper crest is lower for airfoil B, than for airfoil A. This provides a smaller adverse pressure gradient, even for the higher angle of attack (compared to airfoil A) that is necessary to reach the operating point of $C_l = 1$. Table 2 shows that the steady-state and the time-accurate results are in good agreement for airfoil B with a splitter plate.

Figures 11 and 12 show the lift curves and drag polars, respectively, for airfoil B with and without a splitter plate. Figure 11 indicates that the lift is higher for the airfoil without the splitter plate. The splitter plate changes the camber in the trailing edge region and also modifies the Kutta condition. The combined effect is a reduction in the lift for the airfoil with a splitter plate. On the other hand the splitter plate significantly reduces the base drag penalty (Fig. 12), which results in a higher lift-to-drag ratio for airfoil B with a splitter plate. As for airfoil A, strong unsteady vortex shedding occurs,

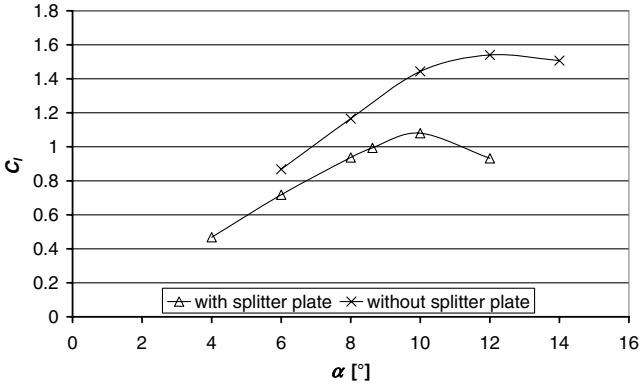

Fig. 11 Lift curves for airfoil B, time-accurate ARC2D simulation, fully turbulent flow, $Re = 1 \times 10^6$, $Ma = 0.3$.

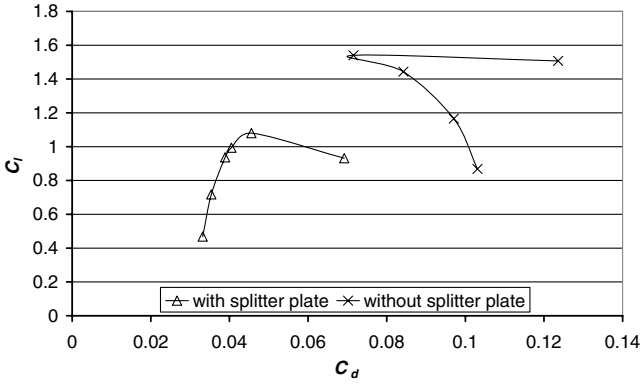

Fig. 12 C_l against C_d polar for airfoil B, time-accurate ARC2D simulation, fully turbulent flow, $Re = 1 \times 10^6$, $Ma = 0.3$.

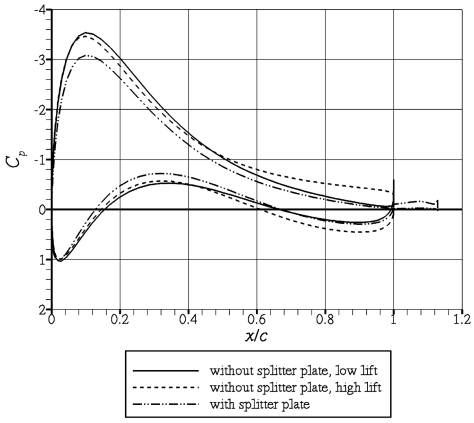

Fig. 13 Comparison of pressure distributions for airfoil B with and without splitter plate at $\alpha = 10$ deg, fully turbulent flow, $Re = 1 \times 10^6$, $Ma = 0.3$.

which results in a large drag penalty. This is not a surprise, because the trailing edge has a thickness of 12.9% of the chord length. Unsteady vortex shedding is reduced for angles of attack of about $\alpha = 12$ deg, as shown by the reduced drag in Fig. 12. Reduced vortex shedding correlates with lower force fluctuations. At $\alpha = 8$ deg the lift oscillates between $C_l = 1.089$ and $C_l = 1.244$, whereas at $\alpha = 12$ deg the amplitude is significantly reduced with the lift oscillating between $C_l = 1.517$ and $C_l = 1.562$.

Figure 13 shows the pressure distribution for airfoil B with and without the splitter plate at $\alpha = 10$ deg. Because of the unsteady flow around the blunt trailing edge, the pressure distribution changes with time. Hence the pressure distribution is plotted for two different periods in time: for the highest and for the lowest lifts appearing during the periodic lift force fluctuations. At $\alpha = 10$ deg, the lift

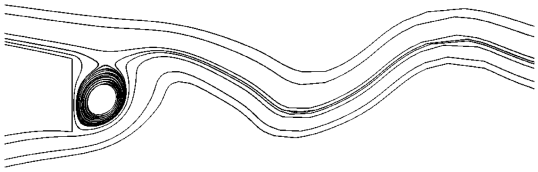

Fig. 14 Instantaneous streamlines at low lift point, airfoil B without splitter plate at $\alpha = 10$ deg, fully turbulent flow, $Re = 1 \times 10^6$, $Ma = 0.3$.

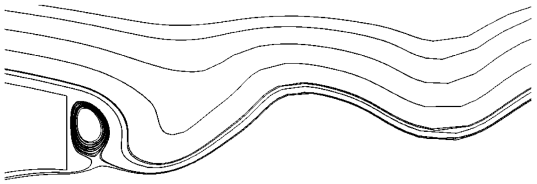

Fig. 15 Instantaneous streamlines at high lift point, airfoil B without splitter plate at $\alpha = 10$ deg, fully turbulent flow, $Re = 1 \times 10^6$, $Ma = 0.3$.

coefficient oscillates between $C_l = 1.382$ and $C_l = 1.507$ for a mean of $C_l = 1.444$.

Figure 14 correlates with the low lift pressure distribution in Fig. 13 and shows a picture of the flow in this state. The vortex at the lower side of the blunt base leads to a flow acceleration on the lower surface, and a deceleration on the upper surface, which results in the low negative pressure coefficient in the rear part of the upper surface, and the low positive pressure in the rear of the lower surface (Fig. 13). $C_l = 1.382$ is the resulting lift coefficient.

Figure 15 correlates with the high lift pressure distribution in Fig. 13. The vortex close to the upper surface accelerates the flow on the upper surface and decelerates it on the lower surface. This results in an incomplete pressure recovery on the upper surface and a higher negative pressure in the rear part of the upper surface, as visible in Fig. 13. The slower flow on the lower surface results in a higher static pressure, in the rear of the lower surface. Overall this incomplete pressure recovery means a significant increase in lift, to a lift coefficient of $C_l = 1.507$.

C. Comparison of Pareto Front Airfoils to the FX77-W Series

To illustrate the advantages of the present airfoil designs, the performance characteristics of airfoil A and airfoil B (both without a splitter plate) will be compared to the airfoils FX77-W-343 and FX77-W-400 (Fig. 2). The FX77-W-343 was introduced in Sec. III. FX77-W-400 is a more truncated thicker version of the FX77-W-343 airfoil. Table 3 lists the moment of inertia, the projected airfoil thickness, and the trailing edge thickness for airfoil A, airfoil B, FX77-W-343, and FX77-W-400.

The aerodynamic data in the following figures are based on time-accurate ARC2D simulations. All airfoils were analyzed for fully turbulent flow conditions at $Re = 1 \times 10^6$ and $Ma = 0.3$. Figure 16 shows the lift curves for the selected airfoils. Based on the geometric characteristics listed in Table 3, airfoil A can be nominally compared to the FX77-W-343 and airfoil B to the FX77-W-400. As shown the Pareto front airfoils generate more lift than the FX77-W airfoils with both the FX77-W-343 and the FX77-W-400 stalling at low angles of attack.

Table 3 Moment of inertia, projected airfoil thickness, trailing edge thickness, for airfoil A, airfoil B, FX77-W-343, FX77-W-400, $Re = 1 \times 10^6$, and $Ma = 0.3$

Airfoil model	I_x	t/c	t_{te}/c
Airfoil A	0.0390	38.2%	9.5%
Airfoil B	0.0473	40.7%	12.9%
FX77-W-343	0.0312	34.6%	4.2%
FX77-W-400	0.0489	40.4%	10.6%

Figure 17 compares the drag polars of the selected airfoils. The airfoils on the Pareto front work at higher lift conditions than the FX77-W series airfoils, which are designed for lower lift conditions as indicated by the lower drag values at low lift conditions.

Figures 18 and 19 compare the lift-to-drag ratios of the selected airfoils as a function of lift coefficient and angle of attack, respectively. Clearly the airfoils from the Pareto front perform much better than the FX77-W airfoils, at least for the fully turbulent flow conditions considered in the present study. Airfoil A provides a significantly higher maximum lift-to-drag ratio than the FX77-W-343, though it has a 25% higher moment of inertia, and airfoil B has a significantly higher maximum lift-to-drag ratio than the FX77-W-400, with both FX77-W airfoils reaching the maximum lift-to-drag ratio at relatively low angle of attack.

Figure 20 shows the pressure distributions for FX77-W-343 and airfoil A at the angle of attack for the best lift-to-drag ratio for each airfoil. The most obvious difference is the lower gradient of the

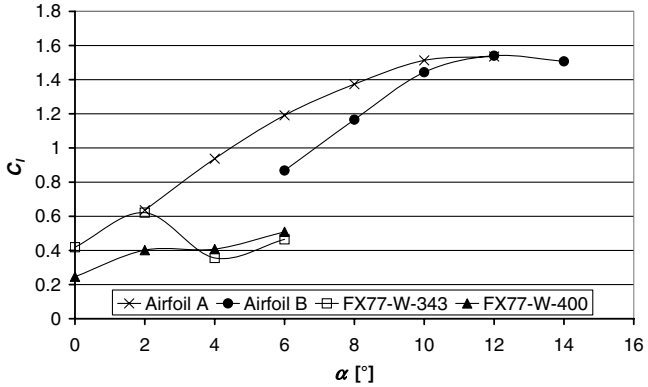

Fig. 16 Comparison of lift curves, time-accurate, fully turbulent flow, $Re = 1 \times 10^6$, $Ma = 0.3$.

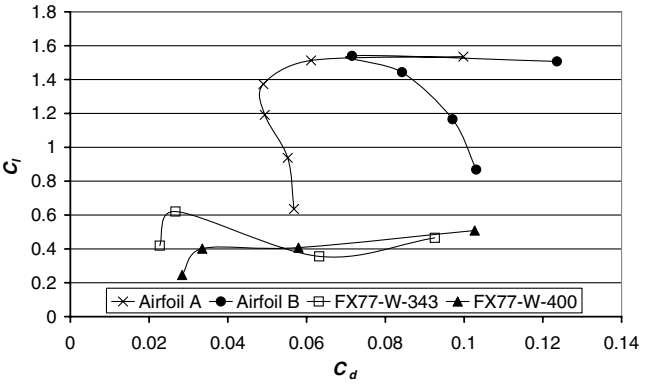

Fig. 17 Comparison of drag polars, time-accurate, fully turbulent flow, $Re = 1 \times 10^6$, $Ma = 0.3$.

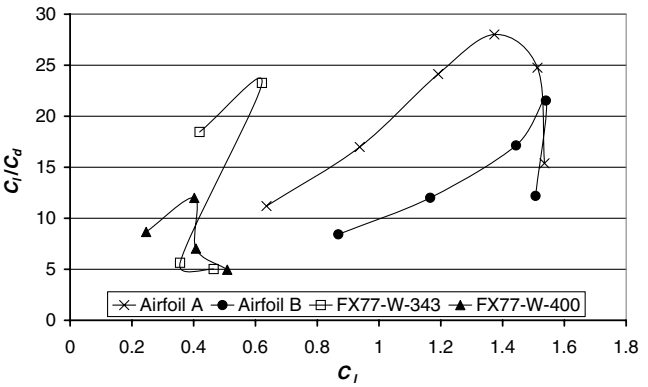

Fig. 18 Comparison of lift-to-drag ratios against lift coefficients, time-accurate, fully turbulent flow, $Re = 1 \times 10^6$, $Ma = 0.3$.

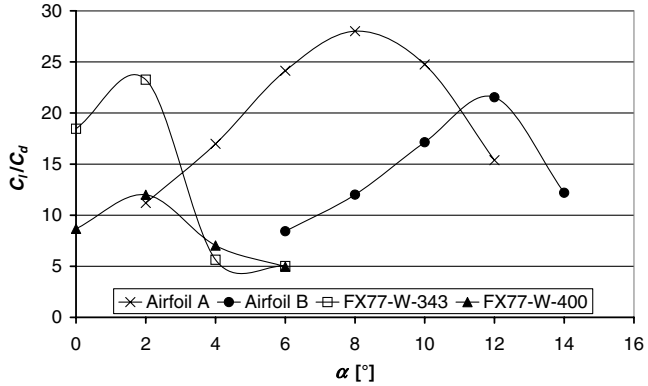

Fig. 19 Comparison of lift-to-drag ratios, time-accurate ARC2D simulation, fully turbulent flow, $Re = 1 \times 10^6$, $Ma = 0.3$.

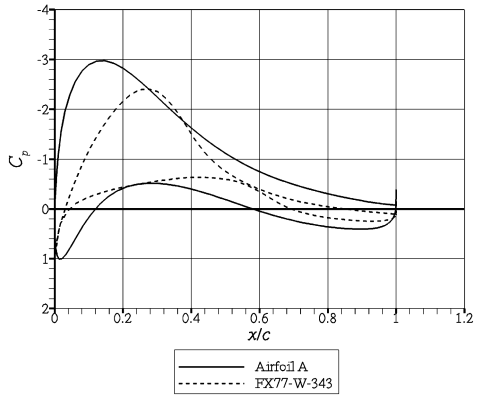

Fig. 20 Comparison of pressure distributions, airfoil A at $\alpha = 8$ deg and FX77-W-343 at $\alpha = 2$ deg, fully turbulent flow, $Re = 1 \times 10^6$, $Ma = 0.3$.

pressure recovery for airfoil A. Though its suction peak is higher than the one of the FX77-W-343, the adverse pressure gradient is kept low, which is an advantage to prevent turbulent separation. This moderate adverse pressure gradient of airfoil A is a product of the optimization for fully turbulent conditions, which correlates with the demand to prevent turbulent separation. A comparison of the pressure distributions of FX77-W-400 and airfoil B shows similar results.

VI. Conclusion

The objective of this project was the design and numerical optimization of thick airfoils including blunt trailing edges at subsonic flow conditions by means of genetic- (GA) and gradient-based numerical optimization in combination with a Navier–Stokes code.

Different types of surface definitions were considered and a modified form of the PARSEC airfoil generator was used because it is a robust airfoil surface generator that provides significant design flexibility. The so-created section shapes were meshed by means of a hyperbolic grid generator. The O-grid topology was considered to be best suited for the expected airfoil geometries. The Reynolds-averaged Navier–Stokes code ARC2D was used to evaluate the aerodynamic performance of the airfoils. A splitter plate was attached to the blunt trailing edge of the airfoils to mitigate unsteady vortex shedding and allow steady-state simulations with ARC2D, which reduces the computational time required for the optimization process. The surface and grid generator, the Navier–Stokes code, the effectiveness of the splitter plates, and the grid spacing were validated before starting the optimization of thick airfoils.

A conjugate direction method was used to generate airfoils with high lift-to-drag ratio at different predefined thicknesses. These airfoils were used as starting points in a genetic multiobjective optimization for lift-to-drag ratio and sectional moment of inertia. The operating point for this optimization was an airfoil lift coefficient of 1 at a Reynolds number of 1×10^6, a Mach number of 0.3, and fully turbulent surface conditions. The design allowed for airfoil thicknesses between 35 and 42% and trailing edge thicknesses from 0.5 to 20%, which gave the optimizer the opportunity to create airfoils with nominally sharp trailing edge.

Because of the nature of the GA, it was possible to create a range of best airfoils, the so-called Pareto front. It presents the airfoils with the best possible combination of aerodynamic and structural performance. The advantages of genetic optimization were demonstrated and the resulting airfoils were shown to have good aerodynamic performance at the fully turbulent design conditions. A remarkable result is that all airfoils on the Pareto front (even the designs on the high lift-to-drag ratio, low moment of inertia side of the front) have a blunt trailing edge, though the GA had the opportunity to create airfoils with nominally sharp trailing edge. This demonstrates that a blunt trailing edge can improve the aerodynamic performance of thick airfoils at subsonic flow conditions.

Future research will focus on numerical flow simulation improvements, further improvements in airfoil performance and mitigation of the aeroacoustic noise resulting from the bluff body shedding through the application of trailing edge modifications, and the application of these airfoils in the inboard region of wind-turbine rotors. The unsteady bluff body wake present in the computations is qualitatively correct, but it is likely that the vortical strength is overpredicted due to the restriction of the flow to two dimensions. Computationally expensive but more sophisticated 3-D turbulence modeling approaches such as detached eddy simulation (DES) may offer some insight into the bluff body wake development. A further 3-D topic could be the analysis and optimization including trailing edge treatments, such as serrated trailing edge, to minimize unsteady vortex shedding. As shown by the results of this study, minimizing the unsteady vortex shedding is a key to further improve the performance of blunt trailing edge airfoils.

Acknowledgments

T. Winnemöller would like to thank the Erich-Becker-Foundation for the support of this project. Both authors would like to acknowledge the help of Eddie Mayda during the various stages of this project.

References

[1] Hoerner, S. F., "Base Drag and Thick Trailing Edges," *Journal of the Aeronautical Sciences*, Vol. 17, No. 10, Oct. 1950, pp. 622–628.

[2] Hoerner, S. F., and Borst, H. V., *Fluid-Dynamic Lift*, Hoerner Fluid Dynamics, Bricktown, NJ, 1985, pp. 2-10, 2-11.

[3] Standish, K. J., and van Dam, C. P., "Aerodynamic Analysis of Blunt Trailing Edge Airfoils," *Journal of Solar Energy Engineering*, Vol. 125, No. 4, Nov. 2003, pp. 479–487.

[4] Jackson, K., Zuteck, M., van Dam, C. P., Standish, K. J., and Berry, D., "Innovative Design Approaches for Large Wind Turbine Blades," *Wind Energy Technology*, Vol. 8, No. 2, 2005, pp. 141–171.

[5] Tanner, M., "A Method for Reducing the Base Drag of Wings with Blunt Trailing Edge," *The Aeronautical Quarterly*, Vol. 23, No. 1, 1972, pp. 15–23.

[6] Tanner, M., "Reduction of Base Drag," *Progress in Aerospace Sciences*, Vol. 16, No. 4, 1975, pp. 369–384.

[7] Sobieczky, H., "Parametric Airfoils and Wings," *Notes on Numerical Fluid Mechanics*, edited by K. Fuji and G. S. Dulikravich, Vol. 68, Vieweg, 1998, pp. 71–88.

[8] Abbott, I. H., Von Doenhoff, A. E., and Stivers, L. S., "Summary of Airfoil Data," NACA TR-824, 1945.

[9] Spalart, P. R., and Allmaras, S. R., "A One-Equation Turbulence Model for Aerodynamic Flows," AIAA Paper 92-0439, Jan. 1992.

[10] Pulliam, T. H., "Solution Methods in Computational Fluid Dynamics," NASA Ames Research Center, 2005.

[11] Beam, R. M., and Warming, R. F., "An Implicit Finite-Difference Algorithm for Hyperbolic Systems in Conservation Law Form," *Journal of Computational Physics*, Vol. 22, No. 1, 1976, pp. 87–110.

[12] Holst, T. L., and Pulliam, T. H., "Evaluation of Genetic Algorithm Concepts Using Model Problems, Part 1: Single-Objective

Optimization," NASA TM-2003-212812, Dec. 2003.
[13] Holst, T. L., and Pulliam, T. H., "Evaluation of Genetic Algorithm Concepts Using Model Problems, Part 2: Multi-Objective Optimization," NASA TM-2003-212813, Dec. 2003.
[14] Vanderplaats, G. N., *Numerical Optimization Techniques for Engineering Design: With Applications*, Mechanical Engineering, McGraw–Hill, New York, 1984, pp. 41–49, 89–92.
[15] Pulliam, T. H., "Efficient Solution Methods for the Navier-Stokes Equations," Lecture Notes for the von Kármán Institute for Fluid Dynamics Lecture Series: Numerical Techniques for Viscous Flow Computation in Turbomachinery Bladings, von Kármán Institute, Rhode-St-Genese, Belgium, 1985.
[16] Chao, D. D., and van Dam, C. P., "Airfoil Drag Prediction and Decomposition," *Journal of Aircraft*, Vol. 36, No. 4, 1999, pp. 675–681.
[17] Barth, T. J., Pulliam, T. H., and Buning, P. G., "Navier-Stokes Computations for Exotic Airfoils," AIAA Paper 85-0109, 1985.
[18] Zingg, D. W., "Low Mach Number Euler Computations," *Canadian Aeronautics and Space Journal*, Vol. 36, No. 3, 1990, pp. 146–152.
[19] Althaus, D., *Niedriggeschwindigkeitsprofile*, Vieweg, Braunschweig, Germany, 1996, pp. 157–161.
[20] Drela, M., "XFOIL: An Analysis and Design System for Low Reynolds Number Airfoils," *Low Reynolds Number Aerodynamics*, Lecture Notes in Engineering, No. 54, edited by T. J. Mueller, Springer–-Verlag, Berlin, 1989, pp. 1–12.
[21] Thompson, B. E., and Lotz, R. D., "Flow Around a Blunt and Divergent Trailing Edge," *Experiments in Fluids*, Vol. 33, No. 3, 2002, pp. 374–383.